Philosophical Magazine,
Vol. 86, No. 10, 1 April 2006, 1355–1372

Taylor & Francis
Taylor & Francis Group

Nanocrystallisation of an $Fe_{44.5}Co_{44.5}Zr_7B_4$ amorphous magnetic alloy

H. F. LI†, D. E. LAUGHLIN‡ and R. V. RAMANUJAN*†

†School of Materials Science and Engineering, Nanyang Technological University, Singapore, 639798
‡Department of Materials Science and Engineering, Carnegie Mellon University, Pittsburgh, PA 15213, USA

(*Received 25 Feb 2005; in final form 22 Sep 2005*)

The crystallisation of amorphous $Fe_{44.5}Co_{44.5}Zr_7B_4$ was investigated using DSC, electrical resistivity, TEM, HRTEM, CBED and VSM. Melt-spun amorphous $Fe_{44.5}Co_{44.5}Zr_7B_4$ crystallised by the primary crystallisation mode: the DSC results showed two exothermal peaks during heating. The electrical resistivity dropped sharply during the crystallisation event, which was consistent with DSC characterisation. From TEM, HRTEM and CBED results, primary crystallisation products which appeared to be clusters of crystals were found to be single crystal precipitates; these crystals formed in a compact dendritic morphology. Direct measurement of nucleation density and volume fraction was carried out using TEM analysis. The nucleation density was found to be high even in the absence of copper addition. The crystal growth was slow when the average size reached around 30 nm; this resulted in a stable nanocrystalline structure. The soft magnetic properties were improved after nanocrystallisation, the magnetic properties were related to the crystalline volume fraction and the Herzer model.

1. Introduction

In order to optimise their performance, materials are required to have improved properties [1]. Nanostructured materials have a number of attractive properties, such as better mechanical properties, reduced density and superior magnetic properties as compared with conventional coarse grained materials [2, 3]; this area has become an important topic of research and attracted considerable research effort. Nanostructured magnetic materials have exhibited superior soft magnetic properties, for example, the recently developed nanocrystalline Finemet, Nanoperm and HiTperm alloys [4]. Such materials have a typical microstructure of nanocrystals embedded in amorphous matrix. Improvement of soft magnetic properties by the formation of nanocrystals is due to the effect of random anisotropy [5] and exchange coupling [6]. Crystallisation from melt-spun amorphous precursors is an important technique to process nanocrystalline magnetic alloys [7–9]. The microstructure crystallised from the amorphous matrix can be controlled by the addition of elements

*Corresponding author. Email: ramanujan@ntu.edu.sg

Philosophical Magazine
ISSN 1478–6435 print/ISSN 1478–6443 online © 2006 Taylor & Francis
http://www.tandf.co.uk/journals
DOI: 10.1080/14786430500380142

such as Cu and Nb in Finemet alloys and the heat treatment conditions such as heating rate, holding temperature and time [10]. In some cases, crystallisation from the amorphous matrix can result in a deterioration of the magnetic properties [11]. Therefore, the study of crystallisation behaviour of amorphous magnetic alloys is necessary to process useful nanostructures or to use amorphous and crystalline magnetic alloys at elevated temperatures [12–14].

HiTperm alloys (with the compositions $(Fe, Co)_{88}M_7B_4Cu_1$, M = Nb, Hf, or Zr) have significant potential in high temperature and power electronic applications because they retain their high magnetisation and permeability up to high temperatures [15–20]. Since the development of Finemet alloys, Cu has been considered to be an important alloying element; its role is significant in increasing the nucleation density in Finemet alloys [8]. HiTperm alloys were also alloyed with Cu with the aim of increasing the nucleation density. However, it was reported that Cu did not precipitate as clusters prior to the crystallisation of amorphous $Fe_{44}Co_{44}Zr_7B_4Cu_1$ [21], unlike in Finemet and Nanoperm alloys. Hence, the hypothesis that Cu is not needed in this class of alloys was investigated in this paper through characterisation of the crystallisation behaviour of a copper free FeCo based HiTperm magnetic alloy with the composition $Fe_{44.5}Co_{44.5}Zr_7B_4$.

The crystallisation behaviour of this Cu free $Fe_{44.5}Co_{44.5}Zr_7B_4$ amorphous alloy was studied using DSC, electrical resistivity measurement and TEM. Detailed microstructural observation and direct measurements under TEM were carried out in this work to investigate the crystallisation process and its effect on magnetic properties. The improvement of magnetic properties due to nanocrystallisation is also discussed, in the context of the Herzer model [5]. This work shows by quantitative TEM observation that even in the absence of copper, high nucleation densities can be achieved and that crystal growth is retarded beyond a size of 30 nm. The morphology of the crystalline precipitates is confirmed to be an unusual compact dendritic morphology although it was considered by earlier researchers to be crystal clusters [21]. Importantly, the magnetic properties have been correlated with experimental measurements of crystal size and volume fraction, allowing a comparison with the Herzer model.

2. Experimental procedure

The amorphous ribbon, prepared by single-roll melt-spun technique, was about 50 μm thick and 2.5 mm wide. NETZCH DSC 404C was used to study the as-received amorphous ribbon. Four-probe electrical resistivity measurement was conducted in an argon-atmosphere tube furnace with temperature fluctuation less than 2°C. During the measurement, a thermocouple was placed just under the sample. The as-received ribbon was heat-treated in a vacuum furnace (10^{-5} Torr). A transmission electron microscope (JEOL 200 kV TEM) was used for the observation of heat-treated samples. For TEM observation, the heat-treated samples were ground slightly and then ion-milled. High-resolution transmission electron microscopy (HRTEM) and convergent beam electron diffraction pattern (CBED) methods were used to study the individual precipitates. The magnetic property measurements of as-spun and heat treated samples were conducted using a vibrating sample magnetometer (VSM, LakeShore 736). An Ni standard sample was used for the

calibration of the magnetic moment; the coercivity of Ni standard sample was 31 Oer (~2470 A/m) from our equipment.

The thin foil thickness was measured using EELS (electron energy loss spectroscopy) and EDX (energy-dispersive X-ray spectroscopy) techniques [22]. EELS thin foil thickness measurement uses the intensity ratio of zero loss peak and plasmon peak in the spectrum, since the inelastic scattered electrons increase with specimen thickness. For very thin specimens only single scattering occurs; the thickness was estimated using the following formula

$$t = \lambda_p \frac{I_p}{I_0} \tag{1}$$

This method is very convenient. However, since EELS and imaging systems cannot be operated simultaneously in our equipment, this method was just used as a cross check for the thickness measurement using EDX technique. In the EDX spectrum, the intensity of the X-ray peak (corresponding to a specific element) varies with thin foil thickness t [22, 23].

$$I_A = I_A^0 e^{-(\mu/\rho)^A_{spec} \cos(\psi)\rho(t/2)} \tag{2}$$

where I_A is the actual X-ray intensity, $I_A^0$is the generated intensity of X-rays of element A, $(\mu/\rho)^A_{spec}$ is the mass absorption coefficient for the X-ray line of element A by the specimen, ψ is the take off angle and ρ is the specimen density. $(\mu/\rho)^A_{spec}$ is the sum of the mass absorption coefficients for each element times the weight fraction of that element, i.e.

$$\left(\frac{\mu}{\rho}\right)^A_{spec} = \sum_i \left(\frac{C_i \mu}{\rho}\right)^A_i \tag{3}$$

C_i is the weight fraction of element i in the specimen. Values of (μ/ρ) can be found in reference [24]. The I_A^0 in equation (2) can be calibrated from a foil of a suitable element with known mass thickness ρt. In our case, pure Fe crystalline foil was used for this calibration.

The thickness can then be calculated directly, using equation (2), with I_A^0 calibrated using a foil with known mass thickness, $(\mu/\rho)^A_{spec}$ from [24] and the density of the material. In our calculation, the parameters used are:

Density of $Fe_{44.5}Co_{44.5}Zr_7B_4$ alloy: $\rho_{spec} = 8.15\,\mathrm{g\,cm^{-3}}$;
Take off angle: $\psi = 20^\circ$;
The mass absorption coefficient for the X-ray line K of element Fe by the specimen: $(\mu/\rho)^{\mathrm{FeK}}_{spec} = 98.28\,\mathrm{cm^2\,g^{-1}}$.

The nucleation density N_v and volume fraction f_v can then be calculated using the formulae [25]:

$$N_v = \frac{N_A}{t + D_{ave}} \tag{4}$$

$$f_v = \frac{f_A}{1 + 3t/2D_{ave}} \tag{5}$$

N_A and f_A are the areal nucleation density and volume fraction respectively, which can be directly obtained from micrographs. t is the thin foil thickness of the area

of interest, D_{ave} is the average crystal size. During the retrieving of N_A and f_A from micrographs, all particles providing contrast are included. Since compositional contrast also plays a significant role in the micrographs taken at large magnification, the particles that are off-Bragg conditions can be also distinguished from the amorphous matrix. This counting error is small when nanocrystals are not overlapped in the micrograph.

3. Results

Figure 1 shows the DSC result and relative electrical resistivity of melt-spun $Fe_{44.5}Co_{44.5}Zr_7B_4$ magnetic alloy at elevated temperatures with a heating rate of 10°C/min.

Two exothermal peaks can be observed in the DSC result at peak temperatures of 504°C and 694°C respectively, while the electrical resistivity drops sharply around these temperatures after an initial linear increase with temperature. This indicated primary crystallisation behaviour of the $Fe_{44.5}Co_{44.5}Zr_7B_4$ amorphous magnetic alloy. The derivative curve of electrical resistivity versus temperature is also shown in figure 1; there is a good match of the resistivity result with the DSC result.

The microstructures, as observed in TEM, of samples annealed at 420°C are shown in figure 2. There was an obvious increase in the number and size of crystals as annealing time was increased. From the thickness measurements, the nucleation density and crystalline volume fraction were calculated (figure 3). Initially the nucleation density is of the order of $10^{21}\,m^{-3}$; after sufficient annealing time, the nucleation density is higher, of the order of $10^{22}\,m^{-3}$ (figure 3a).

The crystalline volume fraction increases for an increase in annealing time, especially for samples annealed at 400°C and 420°C (figure 3b); a linear increase in crystalline volume fraction with annealing time is observed in samples annealed

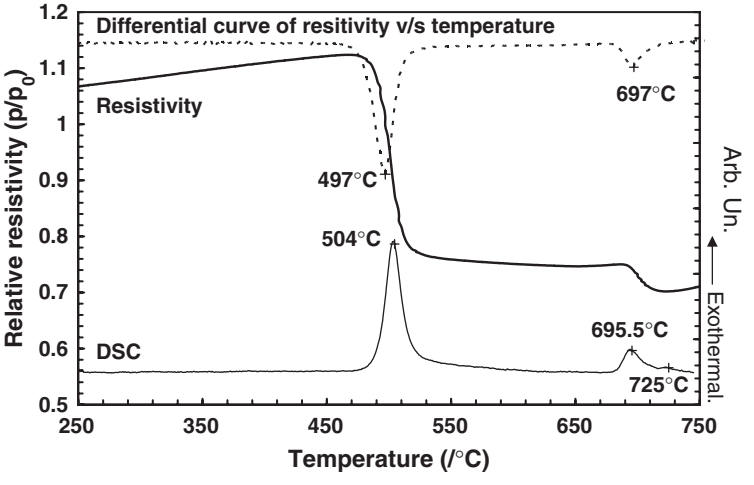

Figure 1. Dynamic electrical resistivity and DSC results of melt-spun amorphous $Fe_{44.5}Co_{44.5}Zr_7B_4$ magnetic alloy at a heating rate of 10°C/min. ρ_0 is the electrical resistivity of amorphous $Fe_{44.5}Co_{44.5}Zr_7B_4$ magnetic alloy at room temperature.

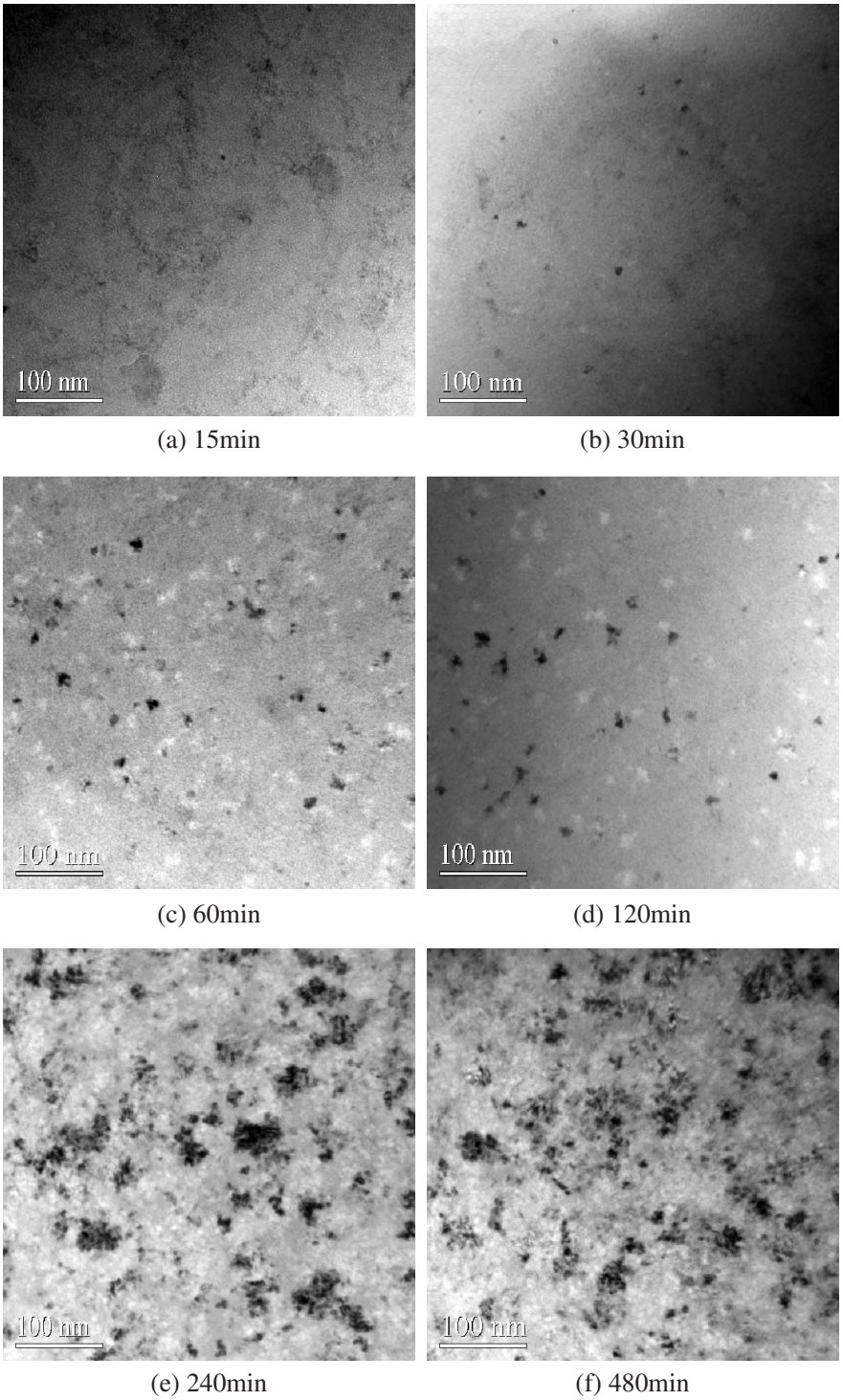

(a) 15min (b) 30min

(c) 60min (d) 120min

(e) 240min (f) 480min

Figure 2. Morphological evolution of melt-spun $Fe_{44.5}Co_{44.5}Zr_7B_4$ alloys when annealed at 420°C.

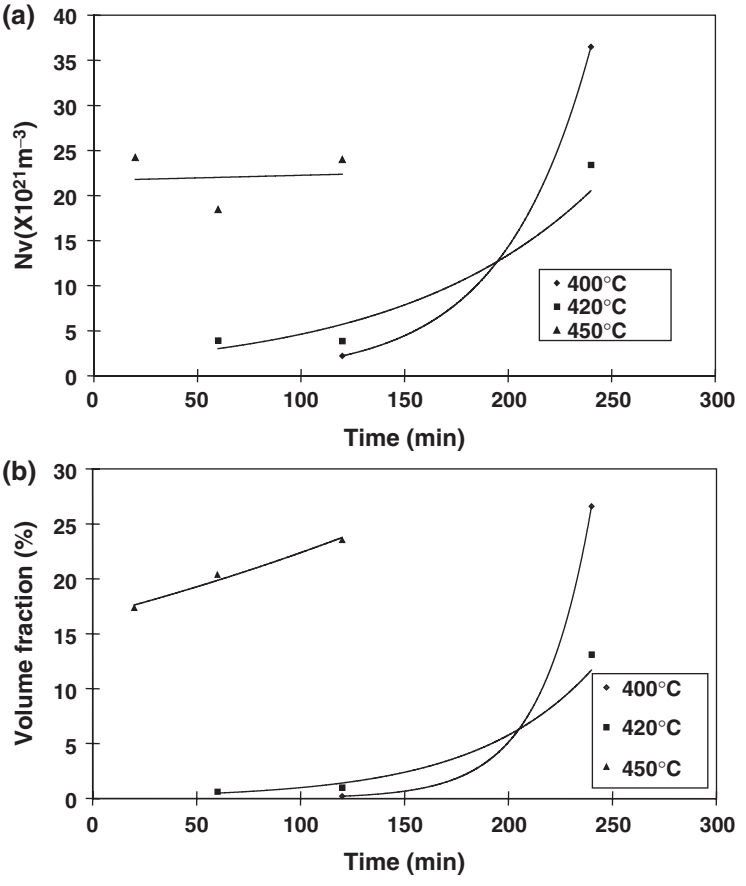

Figure 3. (a) Nucleation density and (b) Crystalline volume fraction of melt-spun $Fe_{44.5}Co_{44.5}Zr_7B_4$ alloys annealed at 400°C, 420°C and 450°C.

at 450°C (figure 3b). Figure 4 shows the morphology of crystals after different heat treatments and the corresponding lattice fringe images. The crystals initially have a relatively regular shape (figure 4a); then they becomes irregular with several sharp corners (figure 4b); finally the crystals are cluster like with a mean size of 20 ~ 30 nm (figure 4c).

From the corresponding lattice fringes, it appears that the crystals with the cluster like features are in fact single crystal. Further evidence is provided in figure 5, which shows crystals and the corresponding CBED patterns. Each CBED contains only a single diffraction pattern, indicating a single crystal. Figure 6 shows the microstructure of a sample annealed at 600°C for 1440 min and a sample annealed at 700°C for 240 min, as well as the corresponding SADP. The size of the crystal is about 40 nm for 600°C 24 h annealing (figure 6a); the crystal size is much larger after 700°C 4 h annealing, being about 100 nm (figure 6b). The corresponding SADPs show that a secondary phase formed after 700°C high temperature annealing and secondary phase was identified to be $(Fe, Co)_3Zr$.

Figure 7 is a plot of the mean size and the size distributions of crystals after annealing. Figure 7a shows the variation of mean size as a function of square root of annealing time at various temperatures, an initial increase of crystal size

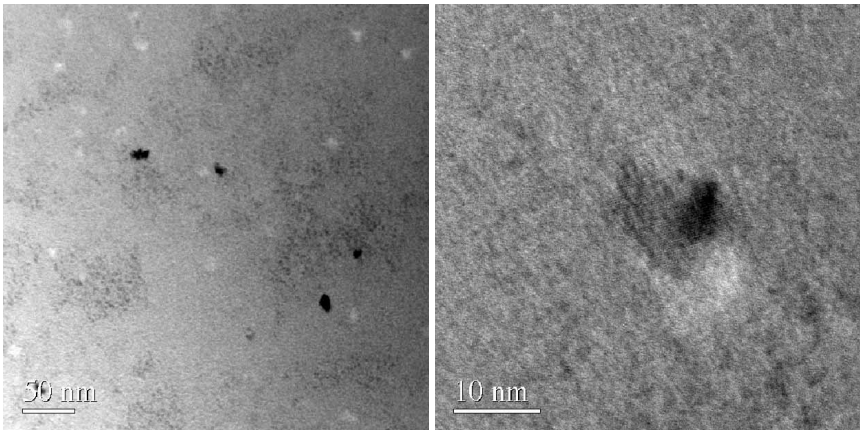

(a) 400°C for 120min

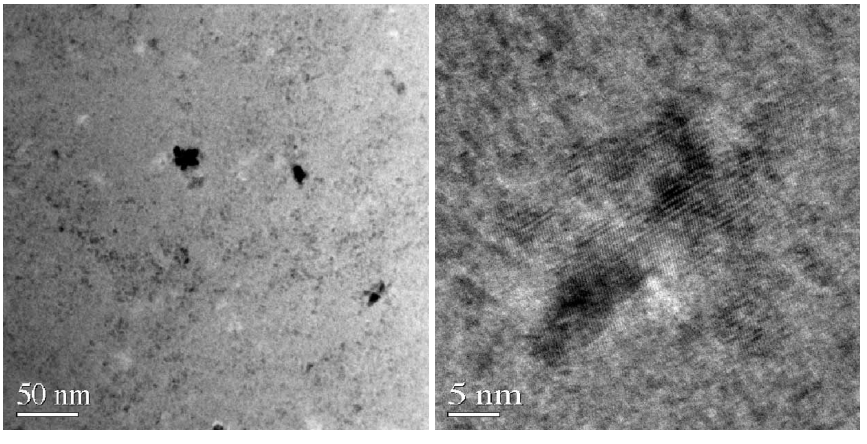

(b) 420°C for 120min

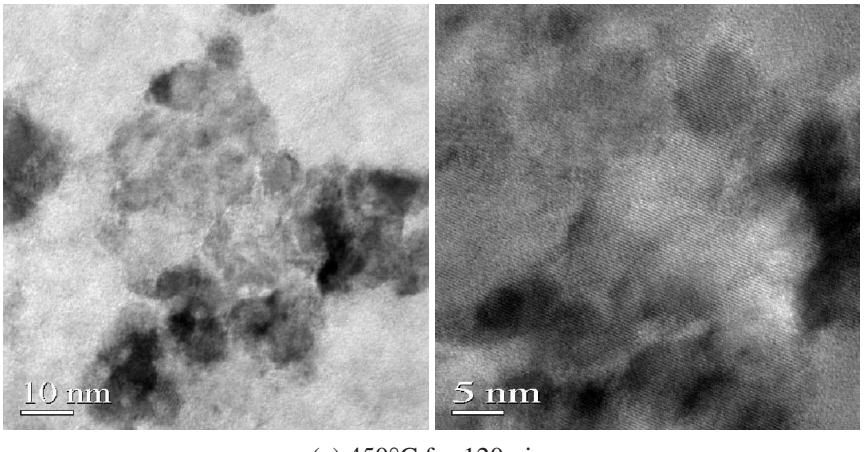

(c) 450°C for 120min

Figure 4. Nanocrystals at different stages and corresponding HRTEM micrographs.

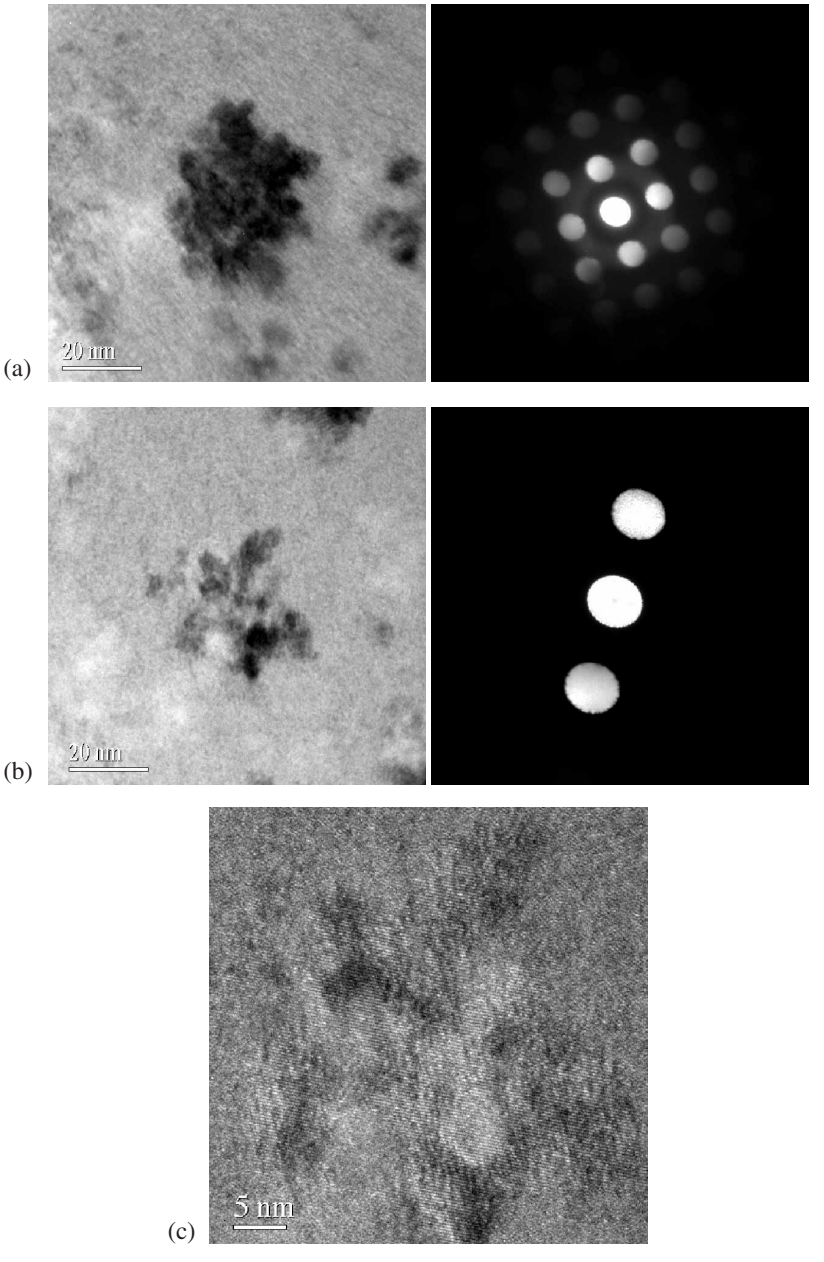

Figure 5. Nanocrystals in the sample annealed at 465°C for 8 h. (a) Nanocrystals and the corresponding CBED with the zone axis [1 0 0], (b) nanocrystals and the corresponding CBED, (c) HRTEM of the crystals in (b).

was observed; however, the increase was slow when the size reached about 20 nm, especially for samples annealed at 465°C and 600°C, and the mean crystal size stabilised at about 30 nm. The crystal size distributions of samples annealed at 450°C in figure 7b showed a Gaussian distribution, with the peak position shifting to larger size and a narrower distribution for longer annealing time.

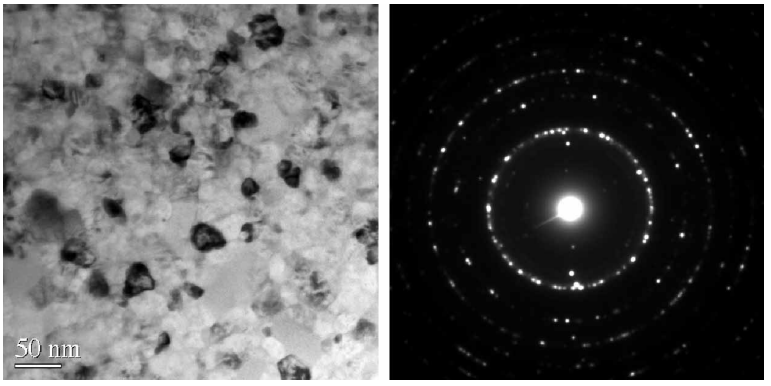

(a)

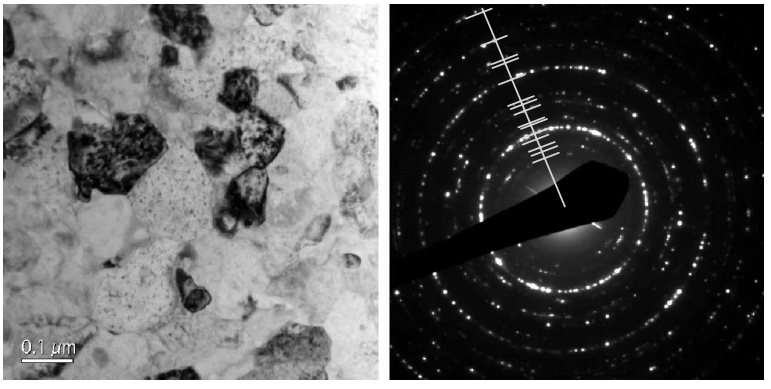

(b)

Figure 6. Morphology of secondary crystallised melt-spun $Fe_{44.5}Co_{44.5}Zr_7B_4$ alloys and the corresponding SADP graphs. (a) 600°C for 1440 min and (b) 700°C for 240 min. From centre to edge, the rings (in SADP of (b)) correspond to 1: $(Fe, Co)_3Zr$ (400), 2: $(Fe, Co)_3Zr$ (331), 3: $(Fe, Co)_3Zr$ (422), 4: $(Fe, Co)_3Zr$ (511), 5: (Fe, Co) (110) and $(Fe, Co)_3Zr$ (440), 6: $(Fe, Co)_3Zr$ (620), 7: $(Fe, Co)_3Zr$ (533) and (622), 8: $(Fe, Co)_3Zr$ (551) and $(Fe, Co)_3Zr$ (731), 9: $(Fe, Co)_3Zr$ (800), 10: (Fe, Co) (200) and $(Fe, Co)_3Zr$ (733), 11: (Fe, Co) (211).

The hysteresis loops of as-spun ribbon and samples annealed at 600°C are shown in figure 8. An increase in coercivity and saturation magnetisation as well as the decrease in the squareness of the loop was observed for the sample annealed at 600°C for 1440 min. For short time annealing or samples annealed at low temperatures, the coercivity and squareness of the loops are comparable with that of as spun ribbon. An example is provided in figure 8, the hysteresis loop of a sample annealed at 600°C for 240 min. The magnetisation and coercivity of the as spun and annealed $Fe_{44.5}Co_{44.5}Zr_7B_4$ samples are listed in table 1.

The coercivity measured using our equipment is large compared to the real value, however, the relative magnitude is believable. Relating the crystalline volume fraction and mean crystal size with the magnetic properties, figure 9 was obtained. In figure 9a, the relationship between volume fraction of crystals and saturation magnetisation showed a linearly increasing relationship; in figure 9b, the relationship between the mean size of crystals and coercivity showed that the coercivity decreased with the increase of precipitate size.

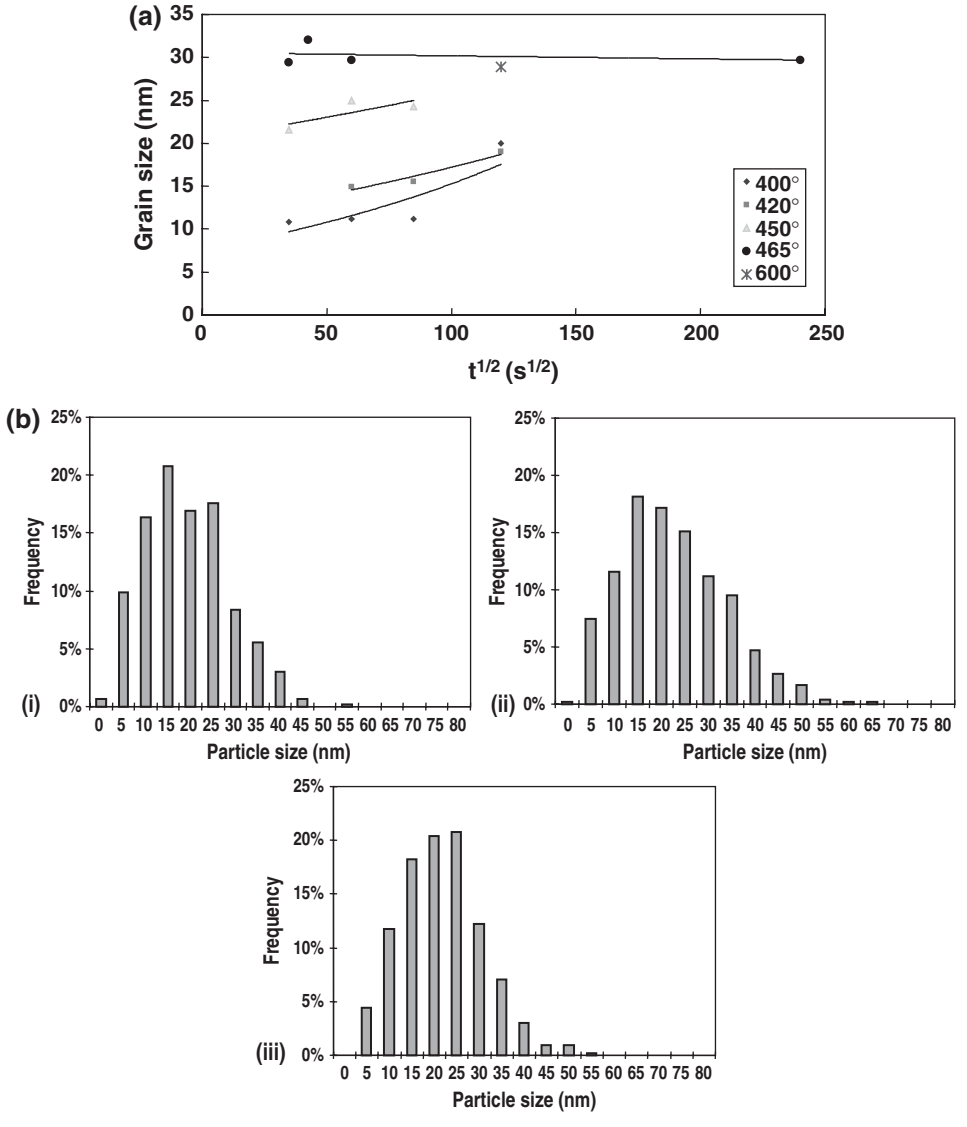

Figure 7. (a) Growth of nanocrystals in primary crystallised $Fe_{44.5}Co_{44.5}Zr_7B_4$ alloys at selected temperatures. (b) Nanocrystal size distribution in primary crystallised $Fe_{44.5}Co_{44.5}Zr_7B_4$ alloys annealed at 450°C for (i) 20 min, (ii) 60 min and (iii) 120 min.

4. Discussion

4.1. *Primary crystallisation behaviour of $Fe_{44.5}Co_{44.5}Zr_7B_4$ amorphous alloy*

DSC and electrical resistivity are two techniques frequently used to study the crystallisation behaviour of amorphous materials [26, 27]. From the DSC curve and dynamic electrical resistivity curve in figure 1, amorphous $Fe_{44.5}Co_{44.5}Zr_7B_4$ displays a primary crystallisation behaviour since there are two exothermal peaks and two sharp drops of electrical resistivity at elevated temperatures. The derivative curve of

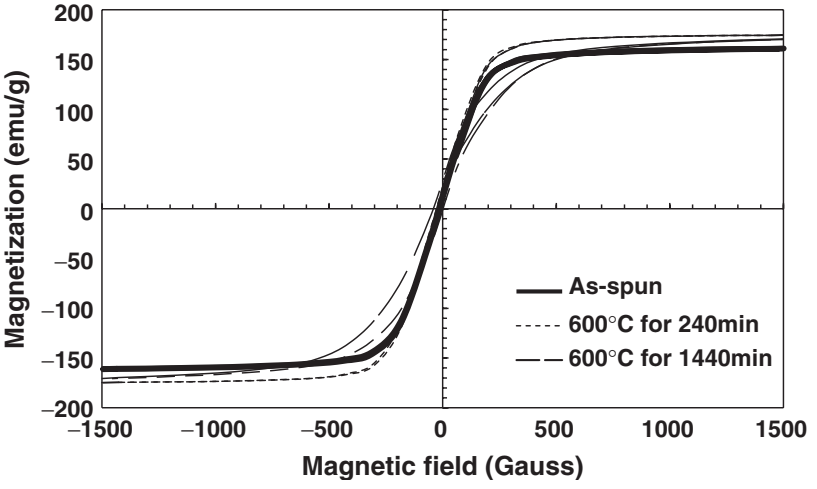

Figure 8. Hysteresis loops of as spun and samples annealed at 600°C.

Table 1. Saturation magnetization (M_s) and coercivity (H_c) of as-spun and samples heat treated from VSM testing.

Heat treatment			
Temperature (°C)	Holding time (min)	M_s (emu/g)	H_c (Oer)
As-spun		163	2.7
400	20	158	4.8
	60	155	5.0
	120	164	5.7
	240	168	4.8
420	15	166	5.5
	30	167	5.0
	60	164	4.6
	120	164	5.3
	240	172	4.2
	480	176	4.0
450	20	170	4.1
	60	176	3.9
	120	178	4.0
465	20	175	4.2
	30	176	3.1
	60	176	3.5
	120	175	4.0
	240	175	4.2
	480	179	4.6
	960	179	3.8
600	30	175	3.9
	60	176	4.2
	120	177	4.3
	240	176	4.4
	480	176	5.8
	1440	181	22.0

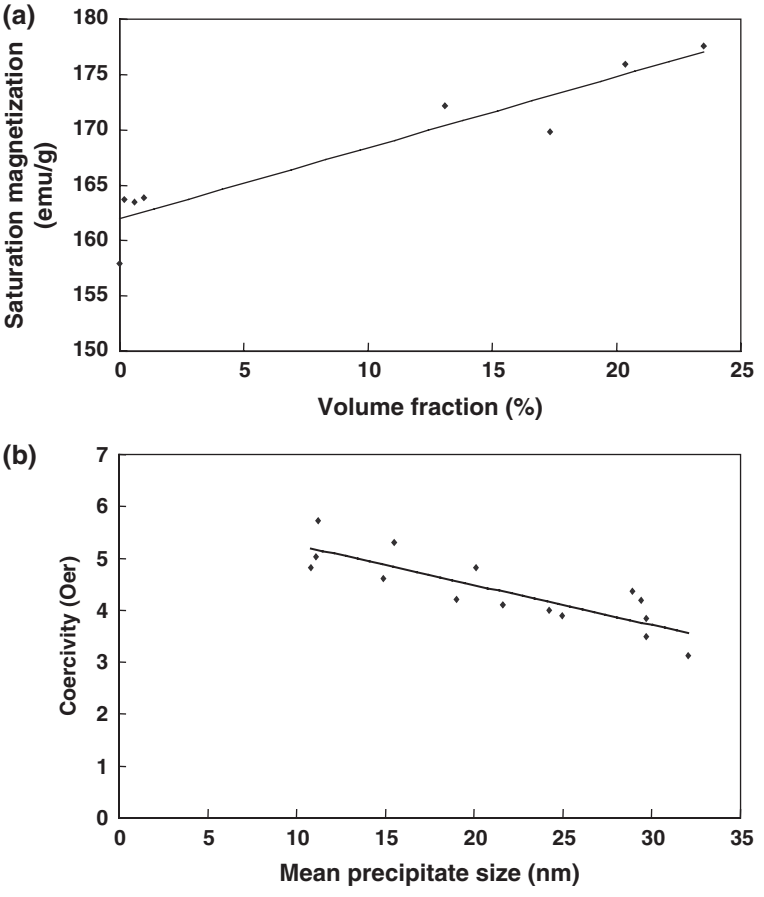

Figure 9. (a) Saturation magnetisation as a function of crystalline volume fraction, (b) coercivity as a function of the mean crystal size in $Fe_{44.5}Co_{44.5}Zr_7B_4$ alloy.

electrical resistivity versus temperature matches the DSC curve very well, indicating that the electrical resistivity has a simple relationship with the crystallisation in $Fe_{44.5}Co_{44.5}Zr_7B_4$ amorphous alloy. From the electrical resistivity curve, the crystalline volume fraction for the primary crystallisation can thus be roughly estimated to be greater than 50%. The slow decrease of electrical resistivity with temperature after primary crystallisation and before the secondary crystallisation event indicated a further ordering, which was considered to be the process of slow consumption of the amorphous matrix by precipitate growth. From the DSC curve, an extra exothermal peak at 725°C was observed after the secondary crystallisation peak of 696°C; it corresponds to a reversible transformation since an endothermal peak can be generally observed in the cooling curve.

The activation energy is an important parameter to characterise the reaction. The activation energies of the primary crystallisation calculated using Kissinger analysis [5, 18] were 3.78 eV/atom and 3.35 eV/atom respectively for copper free $Fe_{44.5}Co_{44.5}Zr_7B_4$ and copper containing $Fe_{44}Co_{44}Zr_7B_4Cu_1$ alloys. The higher activation energy required for primary crystallisation in copper free $Fe_{44.5}Co_{44.5}Zr_7B_4$ alloy indicated that copper seems to aid in the primary crystallisation process.

As reported by Ping [21], Cu did not form clusters or crystalline material, unlike in Finemet and Nanoperm alloys. However, compared to HiTperm alloy with copper addition $Fe_{44}Co_{44}Zr_7B_4Cu_1$ [13], the exothermal peaks did shift to lower temperatures (about 5°C lower) when the heating rate was 0.167°C/s. This result was explained by the suggestion that the Cu addition might decrease the melting point [21]. Since the activation energy was larger in Cu free $Fe_{44.5}Co_{44.5}Zr_7B_4$ than in $Fe_{44}Co_{44}Zr_7B_4Cu_1$, the effect of Cu addition could be to act as a favourable site for heterogeneous nucleation, e.g. by introducing local compositional changes [28].

4.2. *Primary crystallisation of $Fe_{44.5}Co_{44.5}Zr_7B_4$ amorphous alloy from TEM observations*

TEM was used to investigate the crystallisation behaviour of amorphous $Fe_{44.5}Co_{44.5}Zr_7B_4$ alloy. From figure 2, a large increase in the number of precipitates is observed as the holding time becomes longer during the heat treatment: for 15 min heat treatment, only a few precipitates are observed; for 30 min heat treatment, the precipitates are sparse; for 60 min and 120 min heat treatment, the precipitate density is higher, although there is still a large volume fraction of amorphous phase; for 240 min and 480 min heat treatment, the precipitates dominate the microstructure. In figure 2a and b, most of the precipitates have a relatively regular shape, and appear to be single crystal precipitates, but in figure 2c and d, they appear to be irregular clusters [21], however, as discussed in section 4.3, such features were, in fact, single crystal precipitates. With longer annealing time, there was an obvious increase in the size of these precipitates. As shown in figure 2e and f, the size can reach about 60 nm.

Using the thickness data estimated using EDX and EELS techniques, the nucleation density and crystalline volume fraction were calculated (figure 3). From figure 3a, the nucleation density can be as high as $2 \times 10^{22}\,m^{-3}$ for samples annealed at 450°C, and samples annealed at 400°C and 420°C for 240 min. For a relatively short annealing time at 400°C and 420°C, the nucleation densities are lower (less than $5 \times 10^{21} m^{-3}$). Further, for samples annealed at 400°C for 20 min and 60 min, and samples annealed at 420°C for 20 min, only a few precipitates were observed, resulting in much lower nucleation density. These results suggested that nucleation in amorphous $Fe_{44.5}Co_{44.5}Zr_7B_4$ alloy did not follow a constant rate mode, unlike in METGLAS 2826A [29] and some Ni–Ti–B glassy alloys [30]. It has been suggested that if the nucleation stops in a short time, then a fixed number of nucleation sites (quenched-in nuclei) is likely to present [30].

Quantitative analysis had not yet been reported for HiTperm alloys. However, the microstructure of $Fe_{44.5}Co_{44.5}Zr_7B_4$ resembled that of $Fe_{44}Co_{44}Zr_7B_4Cu_1$ alloy [4, 21], indicating that Cu had an indistinct effect on the nucleation density. The nucleation density of this copper free HiTperm $Fe_{44.5}Co_{44.5}Zr_7B_4$ alloy is comparable with that of Finemet alloys ($10^{22}\,m^{-3}$). High nucleation density was also observed during the crystallisation of other amorphous alloy systems in which no elemental additions were used as heterogeneous nucleation sites [31–40]. For example, in Al-base alloys, high particle density ($> 10^{20}$) of Al nanocrystals with a size of about 20 nm was observed [31–36], this was attributed to heterogeneous transient nucleation; in Zr–Al–Cu alloys, a high volume fraction (75%) of nanocrystals was obtained in alloys containing Pd [37–40], the formation of a high

volume fraction of nanocrystals was considered to be due to the preferential Zr–Pd cluster formation. A number of other formation mechanisms have been reported, such as quenched-in nuclei, phase separation in the amorphous phase, high density of internal interfaces, structural rearrangements in the melt and other catalyst generation mechanisms, as summarised by Perepezko in a recent publication [35]. In this alloy, the formation mechanism may resemble that in Al based bulk amorphous alloys, i.e. composition fluctuations developed larger groups of atoms during rapid quenching. Although these groups of atoms did not reach steady state to form crystals, they were frozen and served as heterogeneous nucleation sites for crystallisation during reheating.

The crystalline volume fraction (figure 3b) showed a linear increase with time when annealed at 450°C, at this temperature the crystalline volume fraction reached 15%; however this linear relationship did not occur in samples annealed at 400°C and 420°C, where the crystalline volume fraction remained below 15% for the annealing time investigated. This is attributed to the relative importance of nucleation and grain growth during the crystallisation of $Fe_{44.5}Co_{44.5}Zr_7B_4$ amorphous alloy: when the crystalline volume fraction was lower, nucleation dominated and at higher crystalline volume fraction grain growth dominated, this was also reflected in the nucleation density plot in figure 3a.

4.3. *Precipitates, growth of precipitates and stability*

As stated by Ping, the morphology of nanocrystals observed in Cu free HiTperm $Fe_{44.5}Co_{44.5}Zr_7B_4$ is almost same as that in Cu containing alloy [21], both showed a 'clustered' structure. In order to check if the 'cluster' was a single crystal, conventional TEM observations, HRTEM and CBED techniques were used to study the annealed samples. For these observations, many crystals in each sample were checked; typical results are shown in figure 4 and figure 5. In figure 4a, in the early stage of crystallisation, the precipitates have a relatively regular shape and the corresponding HRTEM micrograph indicates that this is a single crystal. At a later stage in figure 4b, when the crystalline density becomes higher and the crystals become larger, the shape of crystals is irregular and a difference in contrast in one crystalline precipitate can be observed. When the crystalline density becomes much higher (about 20%), the precipitates have a size of more than 20 nm (figure 4c) and look like a cauliflower. However, in these later two stages (figure 4b and c), the corresponding HRTEM micrograph shows lattice fringes in the same direction, which indicate that the crystalline precipitates are single crystals. Further evidence is provided in figure 5: the CBED pattern shows only a single diffraction pattern from a precipitate in the thin area (figure 5a). The CBED pattern was interpreted to belong to bcc (Fe, Co) with the zone axis [100]. Figure 5b showed another precipitate, the corresponding single crystal CBED and HRTEM. Therefore, the 'clusters' are in fact single crystals, which grow in a compact dendritic morphology; the difference of contrast within the precipitate is due to the thickness difference in the parts of the precipitate relative to the thin foil. Nanocrystals exhibiting dendritic morphology were also observed in the crystallisation of Al based alloys, such dendrites were considered to be due to interfacial perturbations following the impingement of the diffusion fields of precipitates [32]. Their morphology may be also induced by the anisotropic growth rates in different crystallographic directions,

since the dendrite growth also occurred when the nanocrystals were relatively sparse. The irregular shape may be due to the lower mobility of atoms in an amorphous matrix compared to that in the melt liquid.

The crystalline size as a function of annealing time at several selected temperatures and the precipitate size distribution at 450°C is shown in figure 7. At the low nucleation density stage, the precipitates have a mean size of about 10 nm. With an increase in annealing time, the mean size increases to 30 nm (figure 7a). No obvious $t^{1/2}$ dependence was observed except for annealing at 450°C. This is not surprising in such alloys, it has also been observed in Finemet, Nanoperm and Fe–Ni–B–Mo alloys. There are a number of factors affecting the crystal size, such as composition at the interface, overlapping of diffusion fields, the effect of a high nucleation density reducing the supersaturation for growth etc. However, it is important to point out that the precipitate size stabilised at 30 nm for 465°C annealing, as well as at 600°C for 240 min annealing. The slow grain growth in the later stage of crystallisation is usually attributed to (a) segregation of heavy elements at the crystal/amorphous interface and (b) diffusion field impingement [4, 10, 31, 32]. In this alloy, it might be due to the high nucleation density coupled with a rejection of solute to the residual amorphous matrix. This decreases the driving force for further nucleation and growth, thus stabilising the microstructures. Ping [21] has reported the composition difference in primary precipitates and remaining amorphous matrix of $Fe_{44}Co_{44}Zr_7B_4Cu_1$ alloy: Zr-enriched residual amorphous phase and Zr-depleted precipitates. The Zr enriched residual amorphous phase will be a composition barrier for the further growth of the primary precipitates. The size distribution showed a Gaussian distribution (figure 7b). For longer annealing time, the peak position shifts to larger size and the size distribution range becomes narrower. While the shift of peak position is small, it again indicates that the growth of precipitates is slow at this stage of crystallisation.

For higher temperature annealing, with increased diffusion, the residual amorphous matrix crystallised. This secondary crystallisation was a heterogeneous nucleation process. As shown in figure 6a, the precipitates did not have a cluster like morphology, unlike those observed in samples annealed at lower temperature or shorter times. This new morphology was produced possibly by consuming the residual amorphous matrix. However, due to the very high density of primary precipitates, and the Zr-enriched regions surrounding the precipitates, the grain growth was slow even at a high temperature of 600°C. This stability will be very useful for high temperature applications of this alloy.

Annealing at 700°C led to the precipitation of $(Fe, Co)_3Zr$, as shown in figure 6b. A large volume fraction of the secondary phases was observed, these phases had a dimension of several nanometers and were uniformly distributed. Compared with the 600°C 1440 min annealed sample, the SADP of the 700°C 240 min annealed sample showed extra rings with much stronger intensities. These extra rings indicated the formation of the $(Fe, Co)_3Zr$ phase. Therefore, the crystallisation process of melt-spun amorphous $Fe_{44.5}Co_{44.5}Zr_7B_4$ alloy begins with the primary crystallisation of (Fe, Co) phase, followed by growth into the remaining Zr-enriched amorphous matrix and finally crystallisation of $(Fe, Co)_3Zr$ from the remaining amorphous matrix. A similar crystallisation process was also favoured in the copper containing $Fe_{44}Co_{44}Zr_7B_4Cu_1$ HiTperm alloy [4, 15–17].

4.4. *Magnetic properties*

The saturation magnetisation (M_s) increased after crystallisation. As shown in figure 8, for samples annealed at 600°C, the saturation magnetisation increased by about 10% and the squareness of the hysteresis loop almost did not change, compared to the amorphous ribbon. However, the hysteresis loop of the sample annealed at 600°C for 1440 min (figure 8) showed smaller squareness of the loop and larger coercivity, which indicated that some of the soft magnetic properties deteriorate after long time and high temperature annealing. This may be due to secondary crystallisation and surface oxidation, as well as an increase in crystal size (as suggested by the Herzer model [5]). The situation for samples annealed at low temperatures or shorter times was better. An example is provided in figure 8: a small increase in squareness of the loop and small increase in coercivity were observed for the sample annealed at 600°C for 240 min. For the crystallised samples, the saturation magnetisation generally increased; the coercivity did not increase much except for the 600°C 1440 min annealed sample. This improvement in soft magnetic properties could be attributed to nanocrystalline formation. This copper free HiTperm alloy has similar magnetisation behaviour to the Cu containing HiTperm alloys which showed a two-step increase in magnetisation after annealing [15], corresponding to primary and secondary crystallisation. The saturation magnetisation under a 10 K Gauss applied field is 170 ~ 180 emu/g for the crystallised samples, the coercivity is in the range of 3 ~ 6 Oer, these values are very close to those of HiTperm alloy with copper addition (for $Fe_{44}Co_{44}Zr_7B_4Cu_1$ alloy, the saturation magnetisation and coercivity were 150 ~ 200 emu/g and 1 ~ 3 Oer respectively [8]). Since Cu is a nonmagnetic element and will decrease the magnetisation when added, and qualitatively, it appears that Cu additions do not have much effect on the microstructure, it is suggested that it need not be added to HiTperm alloys.

The plot of saturation magnetisation as a function of crystalline volume fraction (obtained from TEM observations) showed that M_s increased with the increasing crystalline volume fraction (figure 9a). This is consistent with the saturation magnetisation of a multiphase material being the weight ratio sum of magnetisation of the phases. The coercivity was plotted as a function of crystalline size (figure 9b), which showed that with increasing crystalline size, the coercivity decreased. However, from the Herzer model [5], in the size range selected, the coercivity should be proportional to (crystalline size)^6. This difference in behaviour was considered to be due to the crystalline density effect, since the interaction between the nanocrystalline precipitate will be weak if the neighbouring precipitate distance is larger than the exchange length; it may also be due to the relative large magnetostriction of this alloy.

5. Conclusions

The dynamic and isothermal crystallisation behaviour of Cu free HiTperm $Fe_{44.5}Co_{44.5}Zr_7B_4$ amorphous alloy was investigated using DSC, electrical resistivity measurements, TEM observations and VSM techniques. The major conclusions are:

(a) The amorphous $Fe_{44.5}Co_{44.5}Zr_7B_4$ alloy exhibited primary crystallisation behaviour. The crystallisation temperatures are 504°C and 697°C for

primary and secondary crystallisation processes respectively from DSC analysis. The electrical resistivity shows sharp drops during the crystallisation; the resistivity data matched well with the DSC result.

(b) High-density nanocrystals of (Fe, Co) phase were formed after annealing the amorphous ribbon. The nucleation density was of the order of $10^{22}\,m^{-3}$ from measurements using TEM; significantly the nucleation density was high although no copper has been added to this alloy.

(c) A 'cluster' morphology of crystals was observed by TEM during primary crystallisation of $Fe_{44.5}Co_{44.5}Zr_7B_4$ alloy; this morphology was found from this investigation to arise from single crystals.

(d) It is significant that the growth of crystals was slow when it reached a critical size, typically about 30 nm. This is relevant to microstructural design similar to that performed in Finemet alloys. The stagnation of the increase in crystalline size was attributed to the high density of precipitates and enrichment of Zr in the residual amorphous matrix.

(e) Secondary crystallisation occurred when diffusion was substantial for high temperature annealing at 600°C. This crystallisation occurred by heterogeneous nucleation and by consuming the inter-dendritic residual amorphous matrix. The morphology was no longer 'cauliflower like', unlike the morphology of the samples annealed at lower temperatures or shorter times.

(f) A large volume fraction of the secondary phases $(Fe, Co)_3Zr$ was observed in samples annealed at 700°C for 4 h; the phase had a dimension of several nanometers and was uniformly distributed.

(g) The soft magnetic properties were improved in the primary crystallised samples. The magnetic properties could be correlated in this investigation with the crystalline volume fraction and the mean crystalline size since direct measurements of the two quantities were performed via TEM. Decrease of coercivity with increased crystalline size was observed, which was not expected from the Herzer model; it was considered to be ineffective exchange coupling. The soft magnetic properties deteriorated after secondary crystallisation.

References

[1] J.M.D. Coey, J. Alloys Comp. **326** 2 (2001).
[2] C. Suryanarayana, Intel. Mater. Rev. **40** 41 (1995).
[3] H. Gleiter, Acta Mater. **48** 1 (2000).
[4] M.E. McHenry, M.A. Willard and D.E. Laughlin, Prog. Mater. Sci. **44** 291 (1999).
[5] G. Herzer, J. Magn. Magn. Mater. **112** 258 (1992).
[6] A. Hernando, M. Vázqucz, T. Kulik, *et al*., Phys. Rev. B **51** 3581 (1995).
[7] M.E. McHenry and D.E. Laughlin, Acta Mater. **48** 223 (2000).
[8] M.A. Willard and V.G. Harris, JOM **3** 44 (2002).
[9] A. Makino, A. Inoue and T. Masumoto, Mater. Trans., JIM **36** 924 (1995).
[10] T. Kulik, J. Non-cryst. Solid **287** 145 (2001).
[11] T.Y. Byun, Y. Oh, C.S. Yoon, *et al*., J. Alloy Comp. **368** 283 (2004).
[12] F. Botta, J. Non-cryst. Solids **247** 19 (1999).
[13] J. Friedrich and U. Herr, J. Appl. Phys. **87** 2464 (2000).
[14] H.Q. Guo, H. Kronmuller, T. Dragon, *et al*., J. Appl. Phys. **89** 514 (2001).

[15] M.A. Willard, D.E. Laughlin, M.E. McHenry, *et al*., J. Appl. Phys. **84** 6773 (1998).
[16] M.A. Willard, M.Q. Huang, D.E. Laughlin, *et al*., J. Appl. Phys. **85** 4421 (1999).
[17] M.A. Willard, D.E. Laughlin and M.E. McHenry, J. Appl. Phys. **87** 7091 (2000).
[18] F. Johnson, P. Hughes, R. Gallagher, *et al*., IEEE Trans. Magn. **37** 2261 (2001).
[19] M. Kopcewicz, A. Grabias, M.A. Willard, *et al*., IEEE Trans. Magn. **37** 2226 (2001).
[20] M.D. Graef, M.A. Willard, D.E. Laughlin, *et al*., IEEE Trans. Magn. **37** 2343 (2001).
[21] D.H. Ping, Y.Q. Wu, K. Hono, *et al*., Scripta Mater. **45** 781 (2001).
[22] D.B. Williams and B.C. Carter, *Transmission Electron Microscopy: A Textbook for Materials Science* (Plenum Press, New York, 1996), Chapters 35 and 39.
[23] P.L. Morris, M.D. Ball and P.J. Statham; *Electron Microscopy and Analysis, 1979: Inst. Phys. Conf. Ser. No. 52*, edited by T. Mulvey (The Institute of Physics, Bristol and London, 1979), pp. 413–416.
[24] E.B. Saloman, J.H. Hubbell and J.H. Scofield, X-ray attenuation cross-sections for energies 100 eV to 100 keV and elements $z = 1$ to $z = 90$, At Data Nucl Data Tables **38**(1) 1 (1988).
[25] D.G. Morris, Acta Metall. **31**(10) 1479 (1983); D.G. Morris, Acta Metall. **32**(6) 837 (1984).
[26] M.G. Scott; *Crystallisation in Amorphous Metallic Alloys*, edited by F.E. Luborsky (Butterworth & Co., Cambridge, 1983), p. 144.
[27] J.M. Barandiaran, L.F. Barquin, J.C. Gomez Sal, *et al*., Sol. Stat. Phys. **88** 75 (1993).
[28] A.L. Greer, paper presented in Proc. 22nd RisØ Inter. Symp. Mater. Sci: Science of Metastable and Nanocrystalline Alloys Structure, Properties and Modeling, Denmark (2001), p. 461.
[29] M.V. Heimendahl and G. Kuglstatter, J. Mater. Sci. **16** 2405 (1981).
[30] N. Merk, D.G. Morris and P. Stadelmann, Acta Metall. **35** 2213 (1987).
[31] D.R. Allen, J.C. Foley and J.H. Perepezko, Acta Mater. **46** 431 (1998).
[32] R.I. Wu, G. Wilde and J.H. Perepezko, Mater. Sci. Eng. A **301** 12 (2001).
[33] J.H. Perepezko, R.J. Hebert and W.S. Tong, Intermetallics **10** 1079 (2002).
[34] D.V. Louzguine and A. Inoue, J. Non-crystal. Solid **311** 281 (2002).
[35] J.H. Perepezko, R.J. Hebert and G. Wilde, Mater. Sci. Eng. A **375–377** 171 (2004).
[36] N. Boucharat, H. Rösner, J.H. Perepezko, *et al*., Mater. Sci. Eng. A **375–377** 713 (2004).
[37] C. Li, L. Wang and A. Inoue, J. Phys: Cond. Mater. **13** L803 (2001).
[38] E. Pekarskaya, J.F. Löffler and W.L. Johnson, Acta Mater. **51** 4045 (2003).
[39] A. Inoue and C. Fan, Nanostructured Mater. **12** 741 (1999).
[40] A. Inoue, Prog. Mater. Sci. **43** 365 (1998).